ACS APPLIED MATERIALS & INTERFACES

www.acsami.org

Research Article

# Water Vapor Photoelectrolysis in a Solid-State Photoelectrochemical Cell with $TiO_2$ Nanotubes Loaded with CdS and CdSe Nanoparticles

Xiaolan Kang, Larissa Chaperman, Augustinas Galeckas, Souad Ammar, Fayna Mammeri,* Truls Norby, and Athanasios Chatzitakis*

Cite This: *ACS Appl. Mater. Interfaces* 2021, 13, 46875−46885

Read Online

ACCESS | Metrics & More | Article Recommendations | Supporting Information

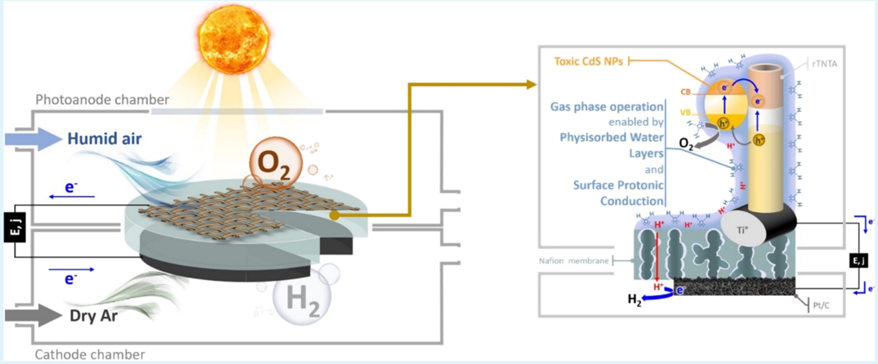

**ABSTRACT:** In this study, polyol-made CdS and CdSe crystalline nanoparticles (NPs) are loaded by impregnation on $TiO_2$ nanotube arrays (TNTAs) for solar-simulated light-driven photoelectrochemical (PEC) water vapor splitting. For the first time, we introduce a safe way to utilize toxic, yet efficient photocatalysts by integration in solid-state PEC (SSPEC) cells. The enabling features of SSPEC cells are the surface protonic conduction mechanism on $TiO_2$ and the use of polymeric electrolytes, such as Nafion instead of liquid ones, for operation with gaseous reactants, like water vapor from ambient humidity. Herein, we studied the effects of both the operating conditions in gaseous ambient atmospheres and the surface modifications of TNTAs-based photoanodes with well-crystallized CdS and CdSe NPs. We showed 3.6 and 2.5 times increase in the photocurrent density of defective TNTAs modified with CdS and CdSe, respectively, compared to the pristine TNTAs. Electrochemical impedance spectroscopy and structural characterizations attributed the improved performance to the higher conductivity induced by intrinsic defects as well as to the enhanced electron/hole separation at the $TiO_2$/CdS heterojunction under gaseous operating conditions. The SSPEC cells were evaluated by cycling between high relative humidity (RH) (80%) and low RH levels (40%), providing direct evidence of the effect of RH and, in turn, adsorbed water, on the cell performance. Online mass spectrometry indicated the corresponding difference in the $H_2$ production rate. In addition, a complete restoration of the SSPEC cell performance from low to high RH levels was also achieved. The presented system can be employed in off-grid, water depleted, and air-polluted areas for the production of hydrogen from renewable energy and provides a solution for the safe use of toxic, yet efficient photocatalysts.

**KEYWORDS:** *solid-state photoelectrochemical cells, water vapor splitting, surface protonic conduction, defects, $TiO_2$ nanotubes, CdS nanoparticles, CdSe nanoparticles*

## ■ INTRODUCTION

As a light emission-free fuel, hydrogen $H_2$ is considered the ultimate alternative to carbon-based energy carriers for industry and transport. Photocatalytic and photoelectrochemical (PEC) water splitting can convert solar energy to $H_2$ directly, a potential future contribution to a hydrogen economy. They are based on the absorption of photon energy by photocatalysts, producing electron−hole pairs that can participate in redox reactions with water.[1,2] PEC $H_2$ production is typically conducted in acidic or alkaline liquid aqueous media, with challenges in cell design, transport, and corrosion. In addition, UV light is partly absorbed by water, and the formation of $H_2$ and $O_2$ bubbles on the electrode surface further leads to overpotentials and scattering of the incident light, decreasing overall efficiency.[3]

Inspired by polymer electrolyte membrane (PEM) fuel cells and electrolyzers, we have previously demonstrated for the first

**Received:** July 10, 2021
**Accepted:** September 15, 2021
**Published:** September 27, 2021

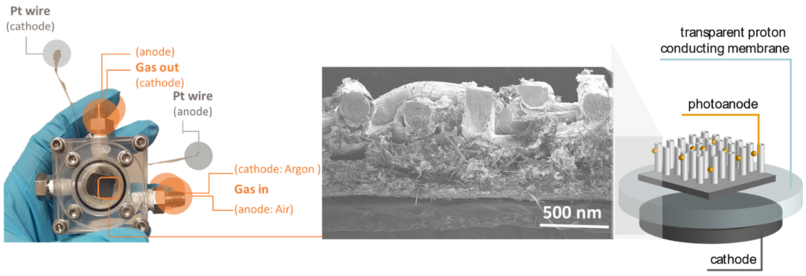

**Figure 1.** Left: SSPEC cell holder and the different parts. Middle: SEM micrograph of the SSPEC cell configuration as well as a schematic representation of the three-layered structure. The top surface of the photoanode electrode is not covered in Nafion in order to allow gas diffusion and surface proton conduction through the adsorbed water layers.

time the photoelectrolysis of water vapor present in ambient humid air in a novel solid-state PEC (SSPEC) cell,[4] comprising a layered structure of an anode, an electrolyte (e.g., Nafion), and a cathode. A key feature in our design for the anode, or more precisely the photoanode operating under gaseous conditions, is that the need of a polymeric binder,[5−9] which allows protonic transport toward the electrolyte, is alleviated.[4] In order to achieve this, we exploited surface proton conduction (SPC), which allows proton ($H^+$) transport in adsorbed water layers on oxide surfaces[10] such as $TiO_2$ by Grotthuss and/or vehicle mechanisms.[11] Compared to liquid PEC cells, the SSPEC design minimizes the distance between two electrodes, making the cell more integral and robust. From an operational point of view, the use of gaseous reactants is also expected to increase the device's durability, transportability, and safety. The absence of liquid electrolytes reduces the risk of environmental contamination from spillage and leaching of toxic components. Furthermore, capturing moisture from air can facilitate large-scale solar $H_2$ production in rural and off-grid areas as the only requirements are humidity and sunlight.

In engineering SSPEC cells, the photoanode should be highly porous to facilitate diffusion, adsorption, and dissociation of water vapor, ensuring a high SPC and triple-phase contact area (electrode−electrolyte−gas phase) for efficient ionic conduction and charge transfer.[4] A 3D electrode based on $TiO_2$ nanotube arrays (TNTAs) grown on a Ti mesh is a promising candidate for SSPEC photoanodes. Their special one-dimensional structure perpendicularly aligned to the substrate provides a high internal surface area for water adsorption and photocatalytic reactions and a short pathway for electron migration.[10] Furthermore, multiple reflections of light entering and proceeding inside the hollow structure considerably improve their light absorption properties.[12,13]

Synthesis of titania nanotubes by anodization of Ti foil yields good control of geometrical factors, like tube length, pore diameter, and wall thickness.[12] Previous studies mainly focused on the growth of TNTAs on flat Ti foil or glass substrates, but less work has been done on a porous and curved surface, like Ti meshes, which can act as gas-permeable electrodes in SSPEC cells.

$TiO_2$ is a well-studied photocatalyst with a wide bandgap of 3.2 eV that can absorb only ~4% of the incoming sunlight.[14] The introduction of intrinsic defects (e.g., oxygen vacancies) significantly increases the visible light response of $TiO_2$ due to the formation of new energy states below the conduction band (CB).[15,16] They also act as shallow electron acceptors and improve charge separation.[17] In addition, in order to achieve high PEC efficiency, electrons accumulated on $TiO_2$ nanotubes need to be transferred to the cathode part as fast as possible. Reduction, e.g., by introduction of oxygen vacancies, significantly improves the n-type electronic conductivity of $TiO_2$, a strategy that was followed in this work by annealing the as-formed TNTAs in a 5% $H_2$/Ar atmosphere (reducing conditions).

Additionally, coupling $TiO_2$ with a narrow bandgap semiconductor as a sensitizing agent can further extend the light absorption in the visible region. $TiO_2$/CdS and $TiO_2$/CdSe are typical nanocomposite systems with the optical response region encompassing nearly all of the visible and UV regions.[18] Semiconducting NPs of CdS and CdSe with their tunable bandgaps provide opportunities for harvesting the visible and even infrared regions of solar light. Based on the bulk energy values, the CB of $TiO_2$ is at −0.5 V vs NHE, while for CdS and CdSe, the CB values are around −0.73 and −0.8 V vs NHE, respectively. This energy difference drives electron transfer from CdS (or CdSe) to $TiO_2$.[19]

Due to their low bandgap and thermodynamic instability, CdS and CdSe NPs suffer from photocorrosion during photocatalytic reactions if no sacrificial agents are involved.[20] Toxic $Cd^{2+}$ ions can leach into the aqueous electrolysis solutions.[21] Several studies have highlighted the toxicity of $Cd^{2+}$ ions to a wide range of microorganisms and cells.[22,23] Herein, CdS and CdSe are deposited on previously reduced $TiO_2$ nanotubes arrays (rTNTAs) and operated under gaseous conditions, thus avoiding the possibility of leaching Cd-based sensitized photocatalysts. Two SSPEC configurations were developed with rTNTAs, which were surface-modified by CdS or CdSe NPs. The deposition of the NPs was done by a facile impregnation process. A Pt/C electrocatalyst was used as a cathode and Nafion as the proton-conducting electrolyte. We tested and compared the PEC performance of TNTAsCdS|Nafion|Pt/C and TNTAsCdSe|Nafion|Pt/C SSPEC cells under different relative humidity (RH) conditions. The ability to replenish their performance after operating under a lower RH value was assessed as well. Finally, the water vapor splitting mechanism under different RH conditions was discussed in light of protonic surface diffusion on the photoanode as well as the polymer electrolyte.

## ■ EXPERIMENTAL SECTION

The details of the growth of $TiO_2$ nanotubes on a Ti mesh as well as the synthesis of CdS and CdSe nanocrystals are provided in the Supporting Information (SI), which also contains the list of chemicals and details of physicochemical and photoelectrochemical characterizations. Moreover, all sample definitions and abbreviations are given in the Supporting Information.

**Preparation of the Solid Polymer Electrolyte and Assembly of SSPEC Cells.** The solid polymer electrolyte was prepared by dropcasting 150 $\mu$L of Nafion5 solution onto both sides of Millipore Prefilter paper (pore size: 0.2 $\mu$m) and then leaving it to dry. The SSPEC was assembled by stacking the previously prepared anode, membrane, and cathode using Nafion20 as the gluing agent: the anode adhered to the membrane using 30 $\mu$L of Nafion20 solution, while the cathode adhered with its Pt/C side facing toward the membrane on the opposite side. It is emphasized that while an excess of mesh on the circumference of the photoactive region was fastened with Nafion to provide mechanical adherence, the active surface of the photoanode was kept free from Nafion. As argued later on, protons are conducted along adsorbed water layers on the TNTAs and are transferred in the electrolyte in the triple-phase boundaries with the electrolyte. On the other hand, the Pt/C cathode was flooded with Nafion, which acted not only as the binder but also as a proton-conducting medium, like in PEM fuels cells and electrolyzers. Then, a 13 kPa pressure was applied to the stack for 12 h at room temperature to ensure good adhesion. Prior to adjusting the SSPEC cell on our in-house-made mounting cell, the three-layer membrane was hydrated overnight by placing it in 1 M $H_2SO_4$ solution.

The schematic representation of the custom-made SSPEC device as well as a cross-sectional view of the SSPEC layered configuration is displayed in Figure 1. The nominal geometric area of the TNTAs mesh photoanode was 1 cm$^2$, while the cathode area was kept approx. two times higher (2 cm$^2$).

Detailed schematic information can be found in our previous work[4] and Figure 1, but briefly, the SSPEC cell was mounted on a special, transparent acrylic frame with a quartz window. Two O-rings were used to ensure that there was no gas crossover between the anode and cathode chambers from the circumference of the three-layer membrane. Moreover, the O-rings were equipped with Pt wires in order to establish electrical contacts with each electrode and the potentiostat. Each compartment was connected to a separate gas line with the anode exposed to wet air and the cathode to wet Ar. The gas flow and RH could be controlled individually by in-house gas mixers and humidifiers.

## ■ RESULTS AND DISCUSSION

**Structural, Chemical, and Optical Characterization.** The crystal structure of the samples was characterized by X-ray diffraction (XRD), and the results are presented in Figure 2. All the $TiO_2$ nanotubes display similar XRD patterns, which can be indexed to the pure anatase phase (ICDD No. 98-000-9853, PDF4).[24] The peak intensity of $TiO_2$ decreased significantly after reducing in a 5% $H_2$ atmosphere at 400 °C, reflecting the decreased crystallinity due to lattice disorder by the formation of intrinsic defects,[17] as will be further discussed later. After being combined with CdX (X = S or Se), the XRD patterns do not show the characteristic peaks of CdX, most probably due to the low concentration and the small crystal size of the chalcogenide phases.[18] For reference purposes, the XRD patterns of TNTAs30 after reduction and combination with CdX are presented in Figure S1.

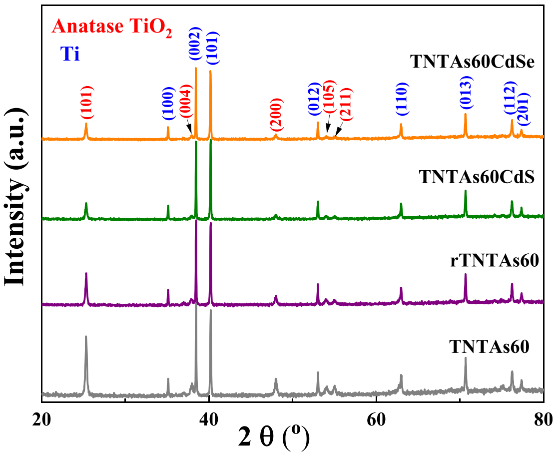

**Figure 2.** XRD patterns of the TNTAs60-based sample series. Peaks with Miller indexes corresponding to the Ti mesh substrate are given in blue and those to anatase $TiO_2$ in red.

The XRD patterns of polyol-made CdS and CdSe NPs are shown in Figure S2. They match very well with the hexagonal wurtzite (ICDD No. 98-003-1490, PDF4)[18] and cubic blende (ICDD No. 98-004-1528, PDF4)[25] structures, respectively. For both, all diffraction peaks appear to be broadened as a consequence of the very small crystal size of the produced chalcogenide phases. The crystal size inferred from Rietveld refinement is found to be about 3 nm.

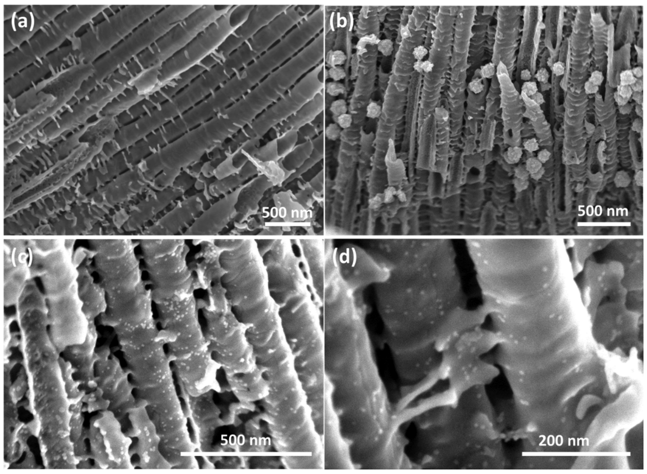

**Figure 3.** Fracture cross-section SEM images of (a) TNTAs60, (b) rTNTAs60CdSe, and (c, d) rTNTAs60CdS. CdS NPs are evenly distributed on the outer surface of the nanotubes, while larger aggregates with much less homogeneous distribution are observed for the CdSe-modified $TiO_2$ nanotubes.

In Figure 3, the fracture cross-section scanning electron microscopy (SEM) images of the rTNTAs60, rTNTAs60CdSe, and rTNTAs60CdS samples are presented. The pore diameter of the as-grown TNTAs60 is around 98 nm, while for TNTAs30, it is approx. 38 nm (Figure S3). The morphology of rTNTAs60 remained identical before and after deposition of CdS, indicating the stable structure of $TiO_2$ nanotubes. Although the XRD pattern of rTNTAs60CdS does not show the peaks of CdS NPs, SEM shows evenly dispersed NPs on the outer walls of the TNTAs. Additional SEM and energy-dispersive spectroscopy (EDS) images for the rTNTAs60 and rTNTAs60CdS samples can be seen in Figure S4. Transmission electron microscopy (TEM) and high-resolution TEM (HRTEM) images of the rTNTAs60CdS sample in Figure S5 clearly show that CdS NPs are attached to the inner and outer surfaces of $TiO_2$ nanotubes (Figure S5c). EDS mapping under dark field mode further confirms the presence of both the Cd and S elements in the rTNTAs60CdS sample (Figure S5d). The HRTEM image of $TiO_2$ in Figure S5e shows that all the lattice fringes are parallel in the same direction with a lattice spacing of 0.24 nm, which fits well with the interplanar spacing of the anatase (004) lattice plane.[26] It is also noticeable that a lattice spacing of 0.337 nm corresponds to the (002) plane of CdS in a wurtzite crystal system.[27]

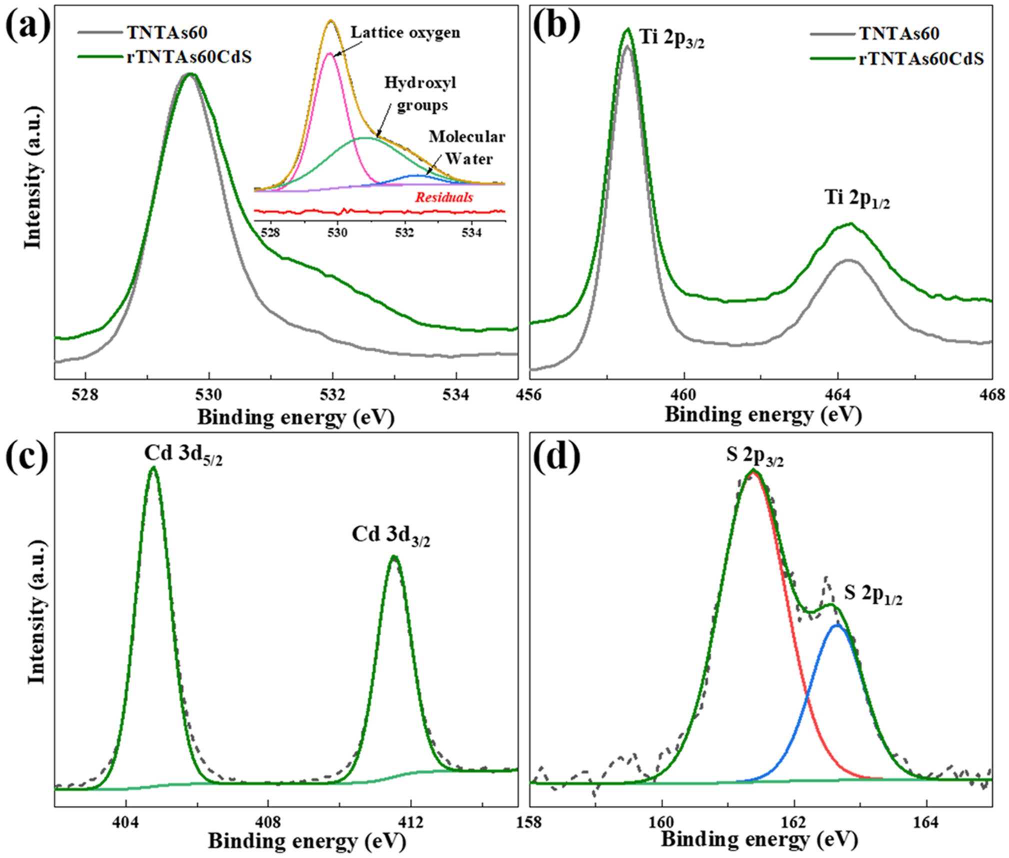

**Figure 4.** XPS spectra and fitted data of TNTAs60 and rTNTAs60CdS: (a) O 1s, (b) Ti 2p, (c) Cd 3d, and (d) S 2p. The inset in (a) shows the peak fitted XPS spectra of O 1s. The peak fitting residuals are also given (red curve).

The as-prepared CdS NPs formed aggregates upon evaporation of the solvent, but they could be separated to a great extent by sonication, leading to small clusters of a few particles, with a total size ranging around 9−10 nm, as shown in Figure S6 (top image). The morphology of the freshly made CdSe-based composites appeared rougher with many smaller-sized nanoparticles forming larger aggregates. The CdSe NPs (Figure S6 bottom image) could not be separated by sonication as was the case with the CdS NPs, and thus they were deposited as large aggregates (approx. 80 nm as given in Figure S7) mainly at the top surface of $TiO_2$ nanotubes. This impacts on the PEC performance of the CdSe-modified TNTAs photoanodes, as we will see later. Finally, fracture cross-section SEM images show the same morphological characteristics between the different samples, and moreover, the length of the nanotubes is approx. 6 $\mu$m (Figure S8).

Amorphous layers, which are generally observed by HRTEM in black $TiO_2$, were not obvious in the reduced $TiO_2$ nanotubes, a possible indication that our $TiO_2$ was not heavily reduced. However, the intrinsic defects can still be manifested by XPS. Figure 4a compares the O 1s core level XPS spectra of TNTAs60 and rTNTAs60CdS, and the sharp peak at 529.7 eV associated to the characteristic peak of lattice oxygen is almost identical for both samples, while a shoulder peak at around 531 eV is much higher in rTNTAs60CdS (Figure 4a inset). This broad peak was deconvoluted and peak fitted with two additional O 1s peaks. The peak at lower binding energies (529.7 eV) is assigned to the hydroxyl groups or nonlattice oxygen (surface adsorbed oxygen), corresponding to Ti-OH. These groups are formed via binding of adsorbed species, like $H_2O$, on oxygen defective sites on the surface of $TiO_2$.[24,28] The second peak at 532.4 eV is ascribed to molecular water adsorbed on the surface of the material.[28,29] Therefore, oxygen vacancies were introduced into rTNTAs60 by annealing in a 5% $H_2$/Ar atmosphere. Two broad peaks centered at 458.5 and 464.3 eV (Figure 4b) correspond to the Ti $2p_{3/2}$ and $2p_{1/2}$ peaks of $Ti^{4+}$ in $TiO_2$, respectively. The absence of shoulder peaks appearing at lower binding energies associated with $Ti^{3+}$ indicates that titanium defects do not exist on the surface of reduced $TiO_2$ nanotubes. The absence of $Ti^{3+}$ in such reduced nanostructured $TiO_2$ has been observed previously and was attributed to the localization of electrons at the vacant oxygen sites.[30,31]

Figure 4c,d reveals the characteristic peaks of CdS dispersed on the surface of rTNTAs60. The high-resolution Cd 3d XPS spectrum displayed two individual peaks of Cd $3d_{5/2}$ and Cd $3d_{3/2}$ at 404.8 and 411.5 eV, corresponding to the $Cd^{2+}$ species in CdS. The deconvoluted peaks of the S $2p_{3/2}$ and S $2p_{1/2}$ signals located at 161.4 and 162.7 eV indicate the presence of $S^{2-}$ in CdS.[18] As for the rTNTAs60CdSe sample, similar results were obtained. Figure S9a shows two peaks located at 405.9 and 412.6 eV for Cd $3d_{5/2}$ and Cd $3d_{3/2}$, respectively. In Figure S9b, the Se 3d component is presented, in which a broad peak at approx. 54.10 eV was fitted with two peaks at 54.02 and 54.90 eV. The difference of 0.88 eV corresponds well to the Se $3d_{5/2}$ and Se $3d_{3/2}$ components of $Se^{2-}$ species, respectively.[32,33] It is worth noting though that the binding energy of the Cd 3d peaks in CdS shifts to lower binding energies than that in CdSe, a fact that is in agreement with a previous report.[34] Moreover, the lower binding energy in the

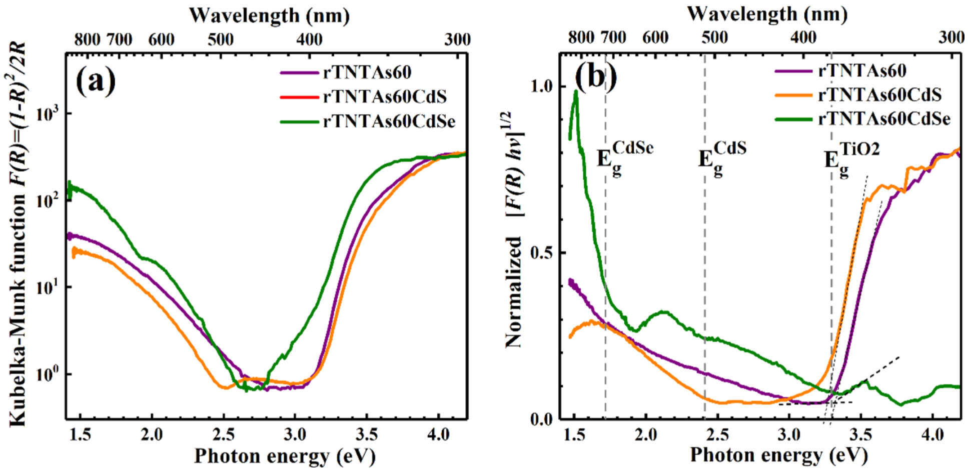

**Figure 5.** Absorption properties of rTNTAs with and without embedded CdS and CdSe NPs. (a) Absorbance spectra represented by the K−M function derived from DRS measurements at 300 K. (b) Tauc plot derived from DRS probed in the region deprived of TNTAs (black-mesh area—see Figure S11). For reference, vertical markers indicate the bandgap positions of the relevant constituents.

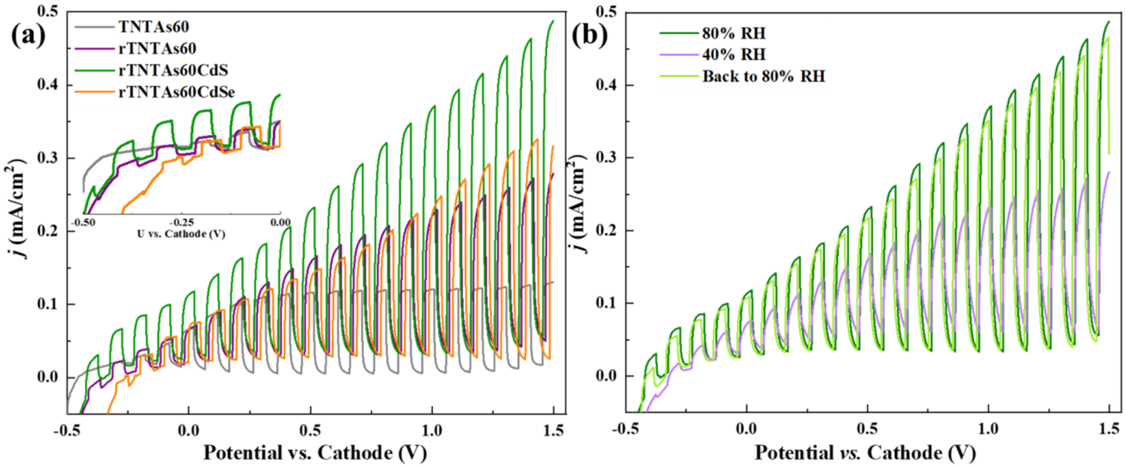

**Figure 6.** LSV plots of the SSPEC cell configurations under one sun illumination. (a) Different photoanodes tested under 80% RH in air. The inset shows a higher magnification at lower applied voltages. (b) rTNTAs60CdS sample tested under different RH levels starting at 80%, then changing to 40%, and finally returning back to 80%. In all cases, the cathode was supplied with 80% RH in Ar.

case of rTNTAs60CdS compared to rTNTAs60CdSe suggests a more intimate interfacial contact between CdS and $TiO_2$.[35]

The absorption and emission properties examined by diffuse reflectance spectroscopy (DRS) and photoluminescence (PL) are summarized in Figure 5 and Figure S10, respectively. The absorption spectra of TNTAs are represented by the Kubelka−Munk (K−M) function in Figure 5a, exposing two distinctive regions of enhanced light coupling. Besides the fundamental absorption (band-edge) region, one can observe a prominent absorption build-up throughout the entire visible range with an onset at 2.5−2.7 eV and a peak at 1.4 eV. The origin of such increased below-bandgap absorption is apparently intrinsic and linked to oxygen vacancies that are abundant in the reduced rTNTAs,[36−38] corroborating very well with the XPS findings. The optical signatures of the embedded CdS and CdSe are not immediately noticeable in the absorption and emission spectra (see Figure S10 and corresponding PL analysis on NPs signatures). Still, the impact from NPs can be perceived by DRS under certain conditions, e.g., while probing NPs-decorated black-mesh areas with no or minimal density of TNTAs that in turn improves the contrast and NPs detection threshold (see Figure S11).

Figure 5b presents the Tauc plot derived from the DRS measurements in such a TNTAs-deprived area, highlighting the $TiO_2$ band-edge at 3.3 eV and certain absorption onsets at around 2.4 and 1.7 eV that can be linked to CdS and CdSe NPs, respectively.[39−41]

### Gas Phase Photoelectrochemical Characterization.

The PEC performances of the different TNTAs-based samples integrated into SSPEC cells were tested with the anode under air of 80% and 40% RH while the cathode was supplied with wet (80% RH) Ar. The linear sweep voltammetry (LSV) curves under intermittent illumination with simulated solar light (100 mW/cm$^2$) are given in Figure 6a. Instant and spike-free photocurrent generation upon chopped illumination is obtained for all the samples, indicating the efficient charge separation in the $TiO_2$ nanotube electrode. Compared to the pristine (TNTAs60) electrode, the photocurrent density of rTNTAs60, rTNTAs60CdS, and rTNTAs60CdSe is enhanced considerably over the entire potential range. In addition, the onset potential of the latter three photoanodes shifted negatively as can be seen from the inset of Figure 6a, suggesting a negative shift in the Fermi level. This is supported by Mott−Schottky measurements that clearly indicate a

https://doi.org/10.1021/acsami.1c13047
ACS Appl. Mater. Interfaces 2021, 13, 46875−46885

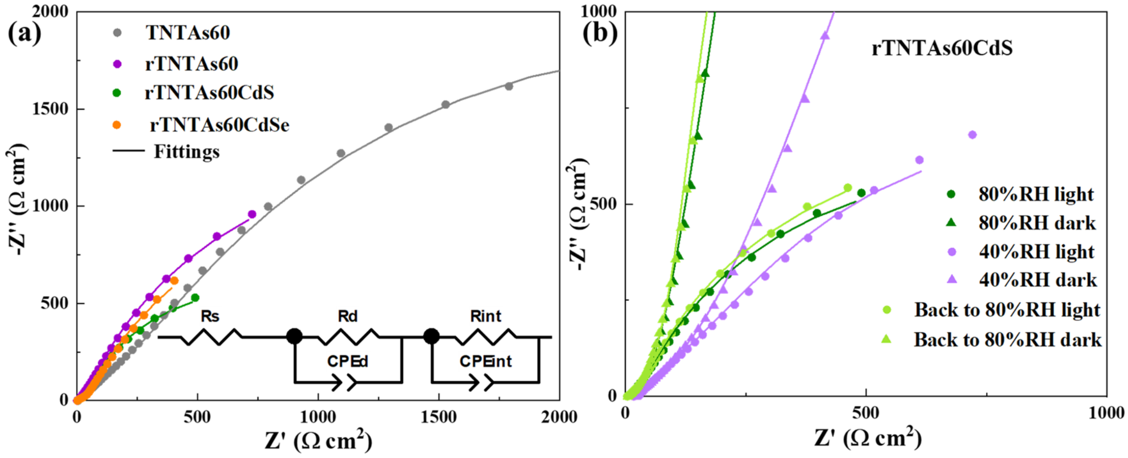

**Figure 7.** Nyquist plots of the SSPEC cell configurations at 1.23 V vs cathode under one sun simulated illumination. (a) Different photoanodes tested under 80% RH in air (inset: the equivalent circuit used to fit the raw data). (b) rTNTAs60CdS initially at 80%, then at 40%RH, and after that, switching back to 80%. A higher magnification in the high frequency region is given in Figure S16. The dots are the raw data, and the lines are the fitted results. In all cases, the cathode was supplied with 80% RH in Ar.

negative shift of the flat band potential of the rTNTAs60CdS photoanode (see Figure S12 and Table S1 and corresponding analysis). The SSPEC configuration with rTNTAs60CdS as the photoanode achieved the highest photocurrent density of 0.44 mA/cm$^2$ at 1.23 V vs cathode under one sun illumination. This performance is 3.6, 1.7, and 1.5 times higher than those of SSPEC cells with TNTAs60, rTNTAs60, and rTNTAs60CdSe as photoanodes, respectively. As a comparison, we chose a pH-neutral electrolyte (0.5 M $Na_2SO_4$) and tested our photoanodes in a typical three-electrode aqueous PEC setup. The results are presented in Figure S13, and we observe the same trend in their PEC performance as in the gas phase operation, with the rTNTAs60CdS sample reaching approx. 0.55 mA/cm$^2$ at 1.23 V vs SCE. This further highlights the high performance achieved by our gas phase PEC system.

It is well-known that the photocurrent and onset potential are closely related to the charge transport and separation and ionic conduction as well as the efficiency of light absorption. When reducing the TNTAs in a 5% $H_2$/Ar atmosphere, oxygen vacancies are introduced, as shown by XPS and DRS/PL earlier, that can be responsible for improving both the conductivity and the visible light response.[15] In addition, both theoretical calculations and experimental results have shown that oxygen vacancies on $TiO_2$ surfaces enhance adsorption and dissociation of water molecules, ultimately increasing the surface protonic conduction.[42−44] It increases the performance of the photoanode also by increasing the concentration of reactants for water splitting.

Additionally, the improved PEC performance can be attributed to the enhanced light-absorbing capacity of rTNTAs60CdS compared to the rest of the samples as witnessed by the incident-photo-to-current-efficiency (IPCE) measurements in Figure S14. It can be seen that the rTNTAs60CdS photoelectrode shows an IPCE of around 3.5 times higher than that of TNTAs60 in the UV light region as well as 2.5 times higher in the visible light range. In the case of the rTNTAs60CdSe photoelectrode, the PEC performance is slightly improved at applied voltages of more than 1.0 V when compared to the rTNTAs60 alone. The CdSe NPs formed large aggregates that were not evenly dispersed on the surface of the TNTAs, leading to an inefficient contact with the nanotubes. This is also supported by the significant positive shift in the Cd 3d$_{5/2}$ and Cd 3d$_{3/2}$ binding energies in the rTNTAs60CdSe sample compared to the rTNTAs60CdS sample as seen earlier by XPS. Therefore, a stronger separation field is needed before the effect of the CdSe NPs can be beneficial.

In order to evaluate the influence of RH on the PEC water vapor splitting, the best performing SSPEC cell with the rTNTAs60CdS photoanode was tested at a reduced water vapor level of 40% RH. As displayed in Figure 6b, the SSPEC cell exhibited a decrease in the performance by a factor of 2. The transient photocurrent response becomes slower too, as the dark current does not reach the background level during the light-off period, implying increased protonic and charge transfer resistances upon dehydration (see the EIS results below). After switching back to 80% RH, the performance is fully recovered.

Similar trends are also observed for the TNTAs30-based photoanodes, as presented in Figure S15. The highest photocurrent density is achieved by using rTNTAs30CdS as the photoanode, which is 2.3 times higher than the SSPEC cell with the TNTAs30 photoanode at 1.23 V vs cathode under one sun illumination. The decrease in the photocurrent density when testing under 40% RH and the ability to recover after switching back to 80% RH highlight again the reversible effects of adsorbed water and the SPC mechanism.

To further study and explain the observed *j*−*E* characteristics of our SSPEC cells, electrochemical impedance spectroscopy (EIS) measurements were carried out in the two-electrode setup under dark and light conditions. The Nyquist results are plotted in Figure 7, along with the suggested equivalent circuit model in the inset of Figure 7a. In the fitted equivalent electrical circuit, $R_s$ is obtained from the intersection of the real axis at the high frequency range and represents the ionic resistance in the electrode and the polymer electrolyte as well as the ohmic resistances (contacts, etc.). Under illumination, two depressed semicircles are observed in the Nyquist plot. The one displayed in the high to mid frequency range (see higher magnification in Figure S16) corresponds to the resistance associated with ionic migration through the polymer electrolyte and the surface proton conduction on the adsorbed water molecules ($R_d$ and $CPE_d$), while the one in the low frequency domain relates to the charge transfer kinetics of

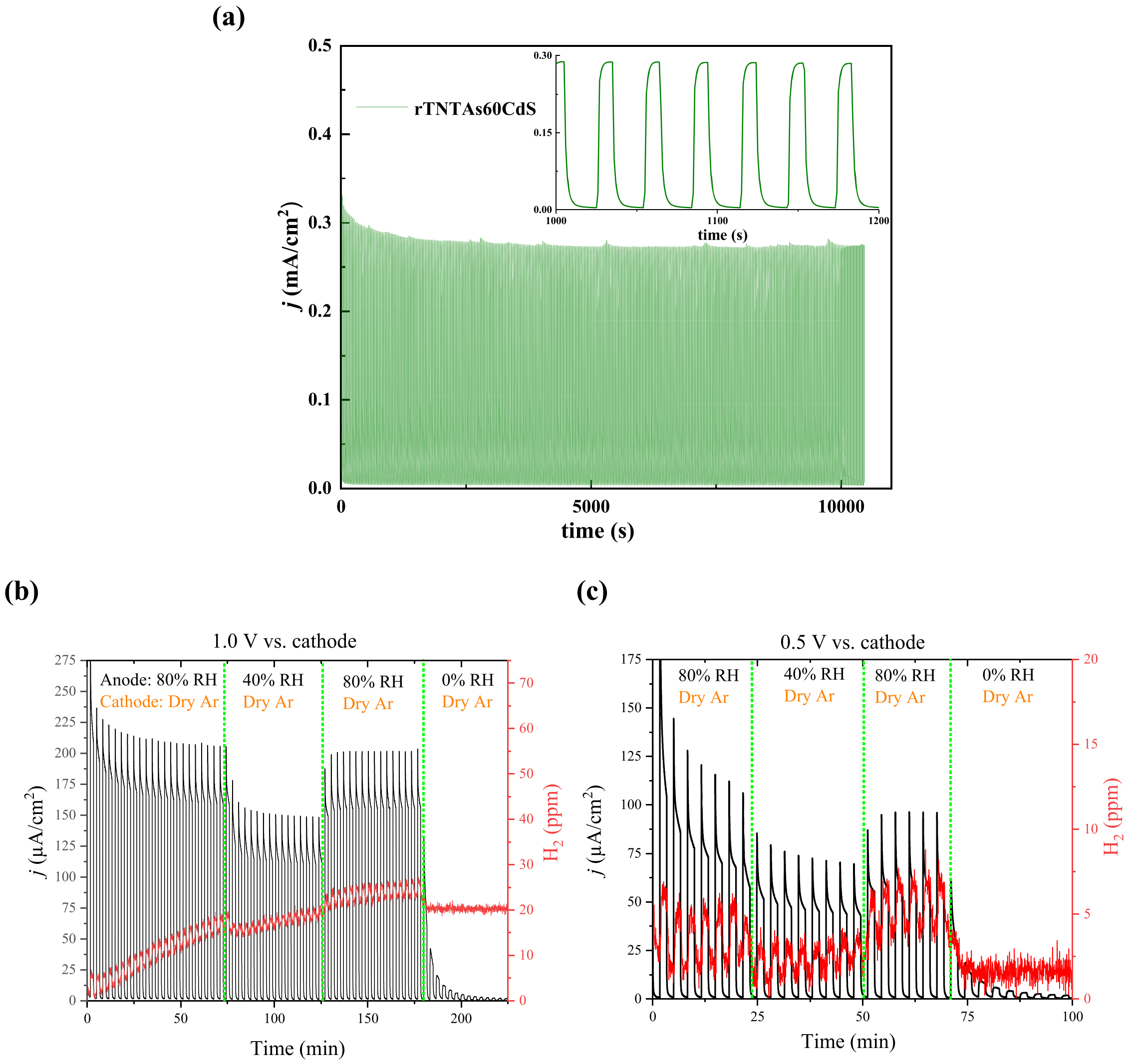

**Figure 8.** Chronoamperometric experiments under different conditions coupled with online mass spectrometry measurements. (a) rTNTAs60CdS photoanode at 1.23 V vs cathode under intermittent one sun illumination at 80% RH. The inset shows a magnification and highlights the on/off cycling. (b) rTNTAs60CdS photoanode at 1.0 V vs cathode and (c) at 0.5 V vs cathode under intermittent one sun illumination and varying RH levels (starting at 80%, switching to 40%, back to 80%, and finally completely dry air conditions). The photoanode was supplied with 40 mL/min of the respective humidified air while the cathode with dry Ar at a flow of 36 mL/min. The sampling rate from the mass spectrometer was 16 mL/min. Higher magnifications at certain regions in (b) and (c) are given in Figure S17.

the water splitting reaction at the interface of the electrode and adsorbed water layers ($R_{ct}$ and $CPE_{ct}$).[45] The resistance and capacitance values are summarized in Table S2.

In comparison to TNTAs60, rTNTAs60 exhibits a significant decrease in the total resistance, which suggests that the efficiency of charge carriers' separation and transport is improved. The reduced overall resistance of the rTNTAs60 photoanode can be attributed to the improved conductivity induced by the surface intrinsic defects. Apparently, the improvement in the SPC, which can be correlated to the $R_d$ component, implies an enhanced water adsorption and dissociation of the rTNTAs60 sample, as suggested earlier. The charge transfer kinetics are further accelerated after surface modification with CdX NPs, and the lowest resistance across the whole frequency range is found in the rTNTAs60CdS configuration. The SPC was also improved after the introduction of the NPs (by a factor of approx. 1.8) but not as significantly as in the case of TNTAs60 and rTNTAs60 (by a factor of 6.5). This is reasonable as the NPs are not fully covering the TNTAs surface. Overall, CdS greatly improves the PEC performance by facilitating the separation and transfer of charge carriers at the photoanode and electrolyte interface, while the reduction of $TiO_2$ accelerated the SPC and related ionic transport.

The kinetic behavior of the best performing SSPEC cells with the rTNTAs60CdS photoanode was further assessed under different conditions (different RH and dark/illumination). As it can be seen in Figure 7b, the charge transfer resistance increases considerably when switching the operating RH from 80% ($R_{ct}$ = 1500 Ω, $R_d$ = 44 Ω) to 40% ($R_{ct}$ = 2760 Ω, $R_d$ = 78 Ω). The SPC depends on water dissociation that produces protonic charge carriers and on their conduction along the formed water layers on the surface of the electrode. A liquid-like water layer establishes at RH above 60%, which induces a remarkable enhancement of proton conduction. At an RH below 60%, the mobility of protonic charge carriers hopping in the chemisorbed water layer and ice-like layer is limited.[11] Therefore, in our case, the conductivity improves apparently after restoring the RH from 40 to 80%. The ionic resistance, $R_s$, of the electrolyte is also increased from 4.1 Ω at 80% to 11.6 Ω at 40% RH because of the higher resistivity of the polymer electrolyte (Figure S16). Again, such a behavior is directly linked to available water molecules and in general the associated resistances increased by a factor of 2 or 3 when the RH, i.e., the available water content, was reduced by half. Another important feature proving that the intermediate to low frequencies are reasonably assigned to charge transfer reactions during the PEC water vapor splitting is derived from EIS being recorded in the dark. A clear capacitive, i.e., blocking, behavior is observed (straight lines parallel to the imaginary axis in the Nyquist plots),[30] as under dark conditions, no interfacial charge transfer reactions (water vapor splitting) are taking place.

The stability of the best performing SSPEC cells with the rTNTAs60CdS photoanode was tested at an applied voltage of 1.23 V (vs cathode) at 80% RH. As shown in Figure 8a, the photocurrent density−time ($j$−$t$) curve reveals a stable and reproducible on/off cycling response to chopped light, especially under the studied conditions where water is not as abundant as in a traditional liquid electrolyte PEC cell. The obtained steady-state photocurrent density agrees well with the LSV curve in Figure 6 (green curve), indicating that the scanning rate in the LSV measurements is sufficiently low. Furthermore, considering that a continuous irradiation heats up the SSPEC cell, this will eventually lead to dehydration of the polymer electrolyte membrane and the photoanode, increasing the resistance for proton conduction. That is the main reason why the chronoamperometric tests are carried out with 10 s light on and 20 s light off (insert of Figure 8a) at a bias potential of 1.23 V vs cathode. In this way, we wanted to ensure that the physisorbed water layers could be compensated during the light-off periods. This was documented and established in previous work from our group, in which the effect of intermittent vs continuous illumination was studied in the photocatalytic remote degradation of organic pollutants.[46] The SSPEC configuration with the rTNTAs60CdS nanocomposite displays a stable photocurrent density after 3 h of operation. However, the photocurrent of pristine TNTAs60 (Figure S18) declines by 37% during the first hour, showing a decreasing trend thereafter. We believe that this behavior is related to the relatively unstable water layers formed on the surface of TNTAs60. As explained earlier, water tends to adsorb molecularly on the surface of pristine $TiO_2$ ($H_2O$−$H_2O$ interactions) and dissociatively on reduced $TiO_2$ (OH−$H_2O$ interactions). The hydrogen bonds between the chemisorbed water layer and physisorbed layer in the pristine sample are less stable than those on the reduced one.[47] As a result, the loosely bonded water network on the pristine surfaces can more easily evaporate upon illumination, ultimately decreasing the available protons and associated PEC performance.

In order to probe the direct $H_2$ production in the gas stream in the cathode side, gas phase analysis was performed by online mass spectrometry. We also wanted to highlight the direct production of dry $H_2$ at relatively low applied bias voltage, and for these reasons, a dry Ar flow was supplied to the cathode with a rate of 36 mL/min and two experiments at 1.0 and 0.5 V (vs cathode) were performed (Figure 8b,c). As the $H_2$ production was expected to be in the ppm level and in order to fit with the mass spectrometer's required dwell and settle times, the light-on/off periods were adjusted to 100 s each. Figure 8b,c show a very good correlation between the amount of water vapor supplied to the photoanode and the obtained photocurrent density as well as the produced $H_2$ at the cathode (refer also to Figure S17, where certain regions have been magnified). It is worth noting that the photocurrent densities at 1.0 and 0.5 V (vs cathode) were lower than the expected ones from the LSV curves of Figure 6, indicating the possible dehydration of the polymer membrane due to the dry Ar feed in the cathode. It is also important to notice that at 0% RH (dry air) in the photoanode, neither photocurrent nor $H_2$ production were observed, correlating perfectly with the proposed surface protonic conduction mechanism.

**Mechanism.** To gain a better overview of the processes happening in our SSPEC cells, we go back and elaborate more of the SPC mechanism and SSPEC cell setup. A detailed schematic and proposed mechanism are presented in Figure 9.

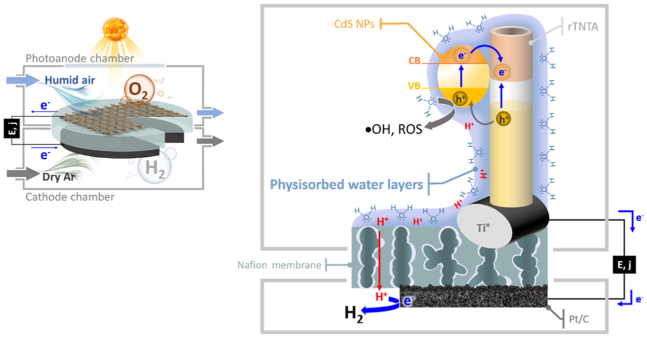

**Figure 9.** Schematic of the SSPEC cell working mechanism with rTNTAs60CdS as the photoanode. The physisorbed water layers on the surface of $TiO_2$/CdS act as a liquid-like electrolyte, where protons can transport and reach the polymer electrolyte (Nafion). The applied voltage provides the necessary electrochemical potential for electrons and protons to reach the cathode catalyst (Pt/C), where $H_2$ is generated. The SSPEC cell can provide pure and dry $H_2$, but due to low temperature operation (25 °C) and to avoid dehydration of the polymer electrolyte, a stream of wet Ar was supplied to the cathode compartment.

$TiO_2$ nanotubes grown on a Ti mesh provide a large surface area and a heterojunction is expected to form between $TiO_2$ and the CdX NPs (let us consider mainly the CdS NPs as they showed the best results) through their physical contact, as proposed from several other studies.[48−50] This is also in agreement with the M−S measurements that showed a negative shift of the flat band potential in the case of the rTNTAs60CdS photoelectrode. Upon illumination, it is expected that the CdS NPs located on the surface of $TiO_2$ nanotubes absorb photons in the visible light range and generate electron−hole pairs. Then, the photogenerated electrons are subsequently injected into the CB of $TiO_2$ due to its lower energy level. Meanwhile, $TiO_2$ nanotubes are also able to absorb photons in the UV region as well as photons in a certain visible light range because of the defect energy levels. The holes migrate to the surface of $TiO_2$ nanotubes that are then transferred to the CdS NPs, where they react with the $H_2O$ molecules in the surface absorbed water layers.

It is also widely accepted that photocatalysts, such as $TiO_2$ and CdS, cannot perform the 4-electron oxidation reaction of water toward oxygen evolution due to poor interfacial kinetics, although their VB energy levels are at the more positive values than the water oxidation standard potential.[51,52] Co-catalysts such as $IrO_2$, $RuO_2$, $Co(OH)_x$, NiFeOOH (layered double hydroxides), etc. that show improved kinetics are necessary for the oxygen evolution reaction (OER).[52] Therefore, the main oxidation products in the case of $TiO_2$ and CdS are expected to be hydroxyl radicals and other reactive oxygen species (ROS) as well as protons.

According to our previous study, a continuous liquid-like water layer forms on the surface of the nanostructured $TiO_2$ at ambient temperatures and under 80% RH.[4] Therefore, protons generated from the water oxidation reaction are transported along the surface water layers, along the surface of nanotubes, and toward the polymer electrolyte. Since Nafion is a known polymeric proton conductor, protons will continue migrating from the photoanode chamber to the cathode chamber through this solid electrolyte. We have measured this effect with EIS, and when the RH was reduced to 40%, then the ionic resistance of the electrolyte increased by a factor of 2.8 (from 4.1 to 11.6 Ω). The applied voltage between the photoanode and cathode provides the necessary electrochemical potential for proton transport toward the cathode electrode. Finally, the electrons are transferred to the counter electrode through the external circuit and participate in the hydrogen evolution reaction by reducing protons on the Pt-based cathode electrode. It is again important to notice that the Ti mesh, which supports the TNTAs layer modified with the CdS NPs, is not flooded by ionomers (Figure 1); that is why our ionic conduction is realized by the adsorbed water layers. In this way, we make sure that the observed photocurrent density is not related to any degradation of the ionomer in contact with the $TiO_2$-based photoelectrode, which could well oxidize the polymeric structure through the photogenerated holes.

## CONCLUSIONS

A robust SSPEC cell of simple engineering was successfully assembled for gas phase PEC water vapor splitting under simulated solar illumination. Such a PEC configuration represents a safe way to utilize toxic, yet efficient photocatalysts, such as CdS and CdSe. The latter was used in the form of NPs prepared by the polyol method and deposited on $TiO_2$ nanotubes grown on a Ti mesh. The mesh morphology was necessary in order to obtain gas-permeable photoanode electrodes. The enabling feature of the gas phase operation is the dual functionality of $TiO_2$, which acts as a photocatalyst and as a surface proton conductor, alleviating the need for an ionomer-coated anode. The surface protonic conduction allows the transport of protons, formed through water vapor photoelectrolysis, toward the polymer electrolyte. The photoelectrocatalytic water splitting properties were improved by sensitization with CdS NPs, and an increase in the photocurrent density by a factor of 3.6 compared to the bare $TiO_2$-based photoanode was achieved. The PEC water vapor splitting performance was evaluated by cycling between high RH (80%) and low RH levels (40%), and it was found that both the protonic and electronic conductivities, which were related to charge transfer reaction kinetics, have almost a proportional dependence with the RH. Previously acquired knowledge highlighted that intermittent illumination is beneficial for long-term operation, as it allows the oxide's surface to stay cool and retain the physisorbed water layers. Such SSPEC cells provide a new method for the safer utilization of toxic materials as well as possible new avenues in order to increase the long-term stability and performance of PEC devices. Finally, the operation with water vapor as the primary feedstock increases their applicability in off-grid, remote areas and regions with humid air of low quality as well as in the utilization of diverse water sources, such as rainwater and wastewater.

## ASSOCIATED CONTENT

### Supporting Information

The Supporting Information is available free of charge at https://pubs.acs.org/doi/10.1021/acsami.1c13047.

> Additional experimental descriptions; additional XRD, TEM, SEM, XPS, and PL results; additional photoelectrochemical measurements including LSVs, Mott−Schottky, IPCE, EIS, and chronoamperometric curves; and tables containing Mott−Schottky- and EIS-extracted values (PDF)

## AUTHOR INFORMATION

### Corresponding Authors

**Fayna Mammeri** − *Interfaces Traitements Organisation et Dynamique des Systèmes (ITODYS), Université de Paris, 75205 Paris, France*; Email: fayna.mammeri@univ-paris-diderot.fr

**Athanasios Chatzitakis** − *Centre for Materials Science and Nanotechnology, Department of Chemistry, University of Oslo, NO-0349 Oslo, Norway*; orcid.org/0000-0001-7193-3236; Email: athanasios.chatzitakis@smn.uio.no

### Authors

**Xiaolan Kang** − *Centre for Materials Science and Nanotechnology, Department of Chemistry, University of Oslo, NO-0349 Oslo, Norway*

**Larissa Chaperman** − *Interfaces Traitements Organisation et Dynamique des Systèmes (ITODYS), Université de Paris, 75205 Paris, France*

**Augustinas Galeckas** − *Centre for Materials Science and Nanotechnology, Department of Physics, University of Oslo, NO-0316 Oslo, Norway*

**Souad Ammar** − *Interfaces Traitements Organisation et Dynamique des Systèmes (ITODYS), Université de Paris, 75205 Paris, France*; orcid.org/0000-0002-1656-0016

**Truls Norby** − *Centre for Materials Science and Nanotechnology, Department of Chemistry, University of Oslo, NO-0349 Oslo, Norway*

Complete contact information is available at: https://pubs.acs.org/10.1021/acsami.1c13047

### Notes

The authors declare no competing financial interest.

X.K. took part in the investigation, validation, methodology, visualization, and writing (original draft, review, and editing). L.C. took part in the investigation, validation, methodology, visualization, and writing (review and editing). A.G. was involved in the investigation and writing (original draft). S.A. was involved in the methodology, resources, visualization, supervision, and writing (review and editing). F.M. took part in the methodology, supervision, writing (review and editing), and funding acquisition. T.N. participated in the conceptualization, methodology, resources, supervision, and writing (review and editing). A.C. participated in the conceptualization, methodology, investigation, visualization, writing (original draft, review, and editing), validation, supervision, project administration, and funding acquisition.

## ■ ACKNOWLEDGMENTS

X.K. acknowledges support from the China Scholarship Council (201806060141). The Research Council of Norway is also acknowledged for support through the projects PH2ON (288320), ATMOS (294681), FUNDAMeNT (251131) and Norwegian Center for Transmission Electron Microscopy, NORTEM (197405). The authors thank Dr. Thomas Aarholt for the TEM measurements.

## ■ REFERENCES

(1) Ding, C.; Shi, J.; Wang, Z.; Li, C. Photoelectrocatalytic Water Splitting: Significance of Cocatalysts, Electrolyte, and Interfaces. *ACS Catal.* **2017**, *7*, 675−688.

(2) Yang, X.; Wang, D. Photocatalysis: From Fundamental Principles to Materials and Applications. *ACS Applied Energy Materials* **2018**, *1*, 6657−6693.

(3) Grimes, C.; Varghese, O.; Ranjan, S., *Light, water, hydrogen: the solar generation of hydrogen by water photoelectrolysis*. Springer Science & Business Media: 2007.

(4) Xu, K.; Chatzitakis, A.; Vøllestad, E.; Ruan, Q.; Tang, J.; Norby, T. Hydrogen from wet air and sunlight in a tandem photoelectrochemical cell. *Int. J. Hydrogen Energy* **2019**, *44*, 587−593.

(5) Iwu, K. O.; Galeckas, A.; Diplas, S.; Seland, F.; Kuznetsov, A. Y.; Norby, T. Effects of temperature, triazole and hot-pressing on the performance of TiO$_2$ photoanode in a solid-state photoelectrochemical cell. *Electrochim. Acta* **2014**, *115*, 66−74.

(6) Stoll, T.; Zafeiropoulos, G.; Tsampas, M. N. Solar fuel production in a novel polymeric electrolyte membrane photoelectrochemical (PEM-PEC) cell with a web of titania nanotube arrays as photoanode and gaseous reactants. *Int. J. Hydrogen Energy* **2016**, *41*, 17807−17817.

(7) Amano, F.; Mukohara, H.; Shintani, A.; Tsurui, K. Solid Polymer Electrolyte-Coated Macroporous Titania Nanotube Photoelectrode for Gas-Phase Water Splitting. *ChemSusChem* **2019**, *12*, 1925−1930.

(8) Iwu, K. O.; Galeckas, A.; Kuznetsov, A. Y.; Norby, T. Solid-state photoelectrochemical H2 generation with gaseous reactants. *Electrochim. Acta* **2013**, *97*, 320−325.

(9) Georgieva, J.; Armyanov, S.; Poulios, I.; Sotiropoulos, S. An all-solid photoelectrochemical cell for the photooxidation of organic vapours under ultraviolet and visible light illumination. *Electrochem. Commun.* **2009**, *11*, 1643−1646.

(10) Scherrer, B.; Schlupp, M. V. F.; Stender, D.; Martynczuk, J.; Grolig, J. G.; Ma, H.; Kocher, P.; Lippert, T.; Prestat, M.; Gauckler, L. J. On Proton Conductivity in Porous and Dense Yttria Stabilized Zirconia at Low Temperature. *Adv. Funct. Mater.* **2013**, *23*, 1957−1964.

(11) Stub, S. Ø.; Thorshaug, K.; Rorvik, P. M.; Norby, T.; Vollestad, E. The influence of acceptor and donor doping on the protonic surface conduction of TiO$_2$. *Phys. Chem. Chem. Phys.* **2018**, *20*, 15653−15660.

(12) Roy, P.; Berger, S.; Schmuki, P. TiO2 Nanotubes: Synthesis and Applications. *Angewandte Chemie International Edition* **2011**, *50*, 2904−2939.

(13) Paramasivam, I.; Jha, H.; Liu, N.; Schmuki, P. A Review of Photocatalysis using Self-organized TiO2Nanotubes and Other Ordered Oxide Nanostructures. *Small* **2012**, *8*, 3073−3103.

(14) Kang, X.; Liu, S.; Dai, Z.; He, Y.; Song, X.; Tan, Z. Titanium Dioxide: From Engineering to Applications. *Catalysts* **2019**, *9*, 191.

(15) Kang, X.; Berberidou, C.; Galeckas, A.; Bazioti, C.; Sagstuen, E.; Norby, T.; Poulios, I.; Chatzitakis, A. Visible Light Driven Photocatalytic Decolorization and Disinfection of Water Employing Reduced TiO2 Nanopowders. *Catalysts* **2021**, *11*, 228.

(16) Chatzitakis, A.; Sartori, S. Recent Advances in the Use of Black TiO2 for Production of Hydrogen and Other Solar Fuels. *ChemPhysChem* **2019**, *20*, 1272−1281.

(17) Kang, X.; Song, X. Z.; Han, Y.; Cao, J.; Tan, Z. Defect-engineered TiO$_2$ Hollow Spiny Nanocubes for Phenol Degradation under Visible Light Irradiation. *Sci. Rep.* **2018**, *8*, 5904.

(18) Hua, J.; Wang, M.; Jiao, Y.; Li, H.; Yang, Y. Strongly coupled CdX (X S, Se and Te) quantum dots/TiO2 nanocomposites for photocatalytic degradation of benzene under visible light irradiation. *Optik* **2018**, *171*, 95−106.

(19) Robel, I.; Kuno, M.; Kamat, P. V. Size-Dependent Electron Injection from Excited CdSe Quantum Dots into TiO2 Nanoparticles. *J. Am. Chem. Soc.* **2007**, *129*, 4136−4137.

(20) Lee, W.; Son, H. J.; Lee, D.-K.; Kim, B.; Kim, H.; Kim, K.; Ko, M. J. Suppression of photocorrosion in CdS/CdSe quantum dot-sensitized solar cells: Formation of a thin polymer layer on the photoelectrode surface. *Synth. Met.* **2013**, *165*, 60−63.

(21) Järup, L.; Åkesson, A. Current status of cadmium as an environmental health problem. *Toxicol. Appl. Pharmacol.* **2009**, *238*, 201−208.

(22) Katsumiti, A.; Gilliland, D.; Arostegui, I.; Cajaraville, M. P. Cytotoxicity and cellular mechanisms involved in the toxicity of CdS quantum dots in hemocytes and gill cells of the mussel Mytilus galloprovincialis. *Aquat. Toxicol.* **2014**, *153*, 39−52.

(23) Paesano, L.; Marmiroli, M.; Bianchi, M. G.; White, J. C.; Bussolati, O.; Zappettini, A.; Villani, M.; Marmiroli, N. Differences in toxicity, mitochondrial function and miRNome in human cells exposed in vitro to Cd as CdS quantum dots or ionic Cd. *J. Hazard. Mater.* **2020**, *393*, 122430.

(24) Kang, X.; Song, X.-Z.; Liu, S.; Pei, M.; Wen, W.; Tan, Z. In situ formation of defect-engineered N-doped TiO2 porous mesocrystals for enhanced photo-degradation and PEC performance. *Nanoscale Adv.* **2019**, *1*, 1372−1379.

(25) Chaguetmi, S.; Chaguetmi, S.; Sobti, N.; Belkahla, H.; Chaperman, L.; Chatzitakis, A.; Achour, S.; Mammeri, F.; Ammar-Merah, S. Enhancement of the photoelectrochemical properties of TiO2 nanofibers supported on Ti sheets by polyol-made CdSe quantum-dots impregnation. *Mater. Lett.* **2020**, *273*, 127934.

(26) Pang, Y.; Xu, G.; Feng, Q.; Lv, J.; Qin, Y.; Zhang, Y.; Zheng, Z.; Wu, Y. Crystalline orientation preference for TiO2 nanotube arrays with efficient photoelectrochemical properties. *Phys. Lett. A* **2018**, *382*, 2759−2762.

(27) Su, C.; Shao, C.; Liu, Y. Electrospun nanofibers of TiO2/CdS heteroarchitectures with enhanced photocatalytic activity by visible light. *J. Colloid Interface Sci.* **2011**, *359*, 220−227.

(28) Wang, Y.; Ren, J.; Wang, Y.; Zhang, F.; Liu, X.; Guo, Y.; Lu, G. Nanocasted Synthesis of Mesoporous LaCoO3 Perovskite with Extremely High Surface Area and Excellent Activity in Methane Combustion. *J. Phys. Chem. C* **2008**, *112*, 15293−15298.

(29) Zhou, W.; Zhao, M.; Liang, F.; Smith, S. C.; Zhu, Z. High activity and durability of novel perovskite electrocatalysts for water oxidation. *Mater. Horiz.* **2015**, *2*, 495−501.

(30) Liu, X.; Carvalho, P.; Getz, M. N.; Norby, T.; Chatzitakis, A. Black Anatase TiO2 Nanotubes with Tunable Orientation for High Performance Supercapacitors. *J. Phys. Chem. C* **2019**, *123*, 21931−21940.

(31) Touni, A.; Liu, X.; Kang, X.; Carvalho, P.; Diplas, S.; Both, K.; Sotiropoulos, S.; Chatzitakis, A., Galvanic Deposition of Pt Nanoparticles on Black TiO2 Nanotubes for Hydrogen Evolving Cathodes. *ChemSusChem* **2021**, accepted article, DOI: 10.1002/cssc.202101559.

(32) Xiao, F.-X.; Miao, J.; Wang, H.-Y.; Yang, H.; Chen, J.; Liu, B. Electrochemical construction of hierarchically ordered CdSe-sensitized TiO2 nanotube arrays: towards versatile photoelectrochemical water splitting and photoredox applications. *Nanoscale* **2014**, *6*, 6727−6737.

(33) Gualdrón-Reyes, A. F.; Meléndez, A. M.; Mejía-Escobar, M. A.; Jaramillo, F.; Niño-Gómez, M. E. The role of boron in the carrier transport improvement of CdSe-sensitized B,N,F-TiO2 nanotube solar cells: a synergistic strategy. *New J. Chem.* **2018**, *42*, 14481−14492.

(34) Vesely, C. J.; Langer, D. W. Electronic Core Levels of the IIB−VIA Compounds. *Phys. Rev. B* **1971**, *4*, 451−462.

(35) Xu, D.; Liu, B.; Zou, W.; Wang, H.; Zhang, C. In situ synthesis of TiO2 nanosheets@CdSe nanocomposites and the improved

photocatalytic performance on removal of methylene blue. *Appl. Surf. Sci.* **2019**, *487*, 91−100.
(36) Serpone, N. Is the Band Gap of Pristine TiO2 Narrowed by Anion- and Cation-Doping of Titanium Dioxide in Second-Generation Photocatalysts? *J. Phys. Chem. B* **2006**, *110*, 24287−24293.
(37) Mathew, S.; Prasad, A. K.; Benoy, T.; Rakesh, P. P.; Hari, M.; Libish, T. M.; Radhakrishnan, P.; Nampoori, V. P. N.; Vallabhan, C. P. G. UV-visible photoluminescence of TiO2 nanoparticles prepared by hydrothermal method. *J Fluoresc* **2012**, *22*, 1563−1569.
(38) Lei, Y.; Zhang, L. D.; Meng, G. W.; Li, G. H.; Zhang, X. Y.; Liang, C. H.; Chen, W.; Wang, S. X. Preparation and photoluminescence of highly ordered TiO2 nanowire arrays. *Appl. Phys. Lett.* **2001**, *78*, 1125−1127.
(39) Murray, C. B.; Norris, D. J.; Bawendi, M. G. Synthesis and characterization of nearly monodisperse CdE (E = sulfur, selenium, tellurium) semiconductor nanocrystallites. *J. Am. Chem. Soc.* **1993**, *115*, 8706−8715.
(40) Baker, D. R.; Kamat, P. V. Tuning the Emission of CdSe Quantum Dots by Controlled Trap Enhancement. *Langmuir* **2010**, *26*, 11272−11276.
(41) Soloviev, V. N.; Eichhöfer, A.; Fenske, D.; Banin, U. Molecular Limit of a Bulk Semiconductor: Size Dependence of the “Band Gap” in CdSe Cluster Molecules. *J. Am. Chem. Soc.* **2000**, *122*, 2673−2674.
(42) Sun, C.; Liu, L.-M.; Selloni, A.; Lu, G. Q.; Smith, S. C. Titania-water interactions: a review of theoretical studies. *J. Mater. Chem.* **2010**, *20*, 10319.
(43) Lang, X.; Liang, Y.; Zhang, J.; Li, L.; Cao, L.; Zhang, H. Structure and reactivity of a water-covered anatase TiO2(001) surface. *Phys. Chem. Chem. Phys.* **2020**, *22*, 1371−1380.
(44) Tilocca, A.; Selloni, A. Structure and Reactivity of Water Layers on Defect-Free and Defective Anatase TiO2(101) Surfaces. *The Journal of Physical Chemistry B* **2004**, *108*, 4743−4751.
(45) Andersen, H.; Xu, K.; Malyshkin, D.; Strandbakke, R.; Chatzitakis, A. A highly efficient electrocatalyst based on double perovskite cobaltites with immense intrinsic catalytic activity for water oxidation. *Chem. Commun.* **2020**, *56*, 1030−1033.
(46) Sun, X.; Xu, K.; Chatzitakis, A.; Norby, T. Photocatalytic generation of gas phase reactive oxygen species from adsorbed water: Remote action and electrochemical detection. *Journal of Environmental Chemical Engineering* **2021**, *9*, 104809.
(47) Henderson, M. A. The interaction of water with solid surfaces: fundamental aspects revisited. *Surf. Sci. Rep.* **2002**, *46*, 1−308.
(48) Gao, X.-F.; Sun, W.-T.; Ai, G.; Peng, L.-M. Photoelectric performance of TiO2 nanotube array photoelectrodes cosensitized with CdS/CdSe quantum dots. *Appl. Phys. Lett.* **2010**, *96*, 153104.
(49) Zhao, G.; Sun, M.; Liu, X.; Xuan, J.; Kong, W.; Zhang, R.; Sun, Y.; Jia, F.; Yin, G.; Liu, B. Fabrication of CdS quantum dots sensitized ZnO nanorods/TiO2 nanosheets hierarchical heterostructure films for enhanced photoelectrochemical performance. *Electrochim. Acta* **2019**, *304*, 334−341.
(50) Khan, U. A.; Liu, J.; Pan, J.; Ma, H.; Zuo, S.; Yu, Y.; Ahmad, A.; Ullah, S.; Li, B. Fabrication of Highly Efficient and Hierarchical CdS QDs/CQDs/H-TiO2 Ternary Heterojunction: Surpassable Photocatalysis under Sun-like Illumination. *Ind. Eng. Chem. Res.* **2019**, *58*, 79−91.
(51) Li, X.; Shen, R.; Ma, S.; Chen, X.; Xie, J. Graphene-based heterojunction photocatalysts. *Appl. Surf. Sci.* **2018**, *430*, 53−107.
(52) Yang, J.; Wang, D.; Han, H.; Li, C. Roles of Cocatalysts in Photocatalysis and Photoelectrocatalysis. *Acc. Chem. Res.* **2013**, *46*, 1900−1909.